Inorganic Chemistry

pubs.acs.org/IC Article

Defect-Accommodating Intermediates Yield Selective Low-Temperature Synthesis of $YMnO_3$ Polymorphs

Paul K. Todd,[O] Allison Wustrow,[O] Rebecca D. McAuliffe,[O] Matthew J. McDermott,[O] Gia Thinh Tran, Brennan C. McBride, Ethan D. Boeding, Daniel O'Nolan, Chia-Hao Liu, Shyam S. Dwaraknath, Karena W. Chapman, Simon J. L. Billinge, Kristin A. Persson, Ashfia Huq, Gabriel M. Veith, and James R. Neilson*

Cite This: *Inorg. Chem.* 2020, 59, 13639−13650 Read Online

ACCESS | Metrics & More | Article Recommendations | Supporting Information

ABSTRACT: In the synthesis of complex oxides, solid-state metathesis provides low-temperature reactions where product selectivity can be achieved through simple changes in precursor composition. The influence of precursor structure, however, is less understood in solid-state synthesis. Here we present the ternary metathesis reaction ($LiMnO_2$ + YOCl → $YMnO_3$ + LiCl) to target two yttrium manganese oxide products, hexagonal and orthorhombic $YMnO_3$, when starting from three different $LiMnO_2$ precursors. Using temperature-dependent synchrotron X-ray and neutron diffraction, we identify the relevant intermediates and temperature regimes of reactions along the pathway to $YMnO_3$. Manganese-containing intermediates undergo a charge disproportionation into a reduced Mn(II,III) tetragonal spinel and oxidized Mn(III,IV) cubic spinel, which lead to hexagonal and orthorhombic $YMnO_3$, respectively. Density functional theory calculations confirm that the presence of Mn(IV) caused by a small concentration of cation vacancies (~2.2%) in $YMnO_3$ stabilizes the orthorhombic polymorph over the hexagonal. Reactions over the course of 2 weeks yield o-$YMnO_3$ as the majority product at temperatures below 600 °C, which supports an equilibration of cation defects over time. Controlling the composition and structure of these defect-accommodating intermediates provides new strategies for selective synthesis of complex oxides at low temperatures.

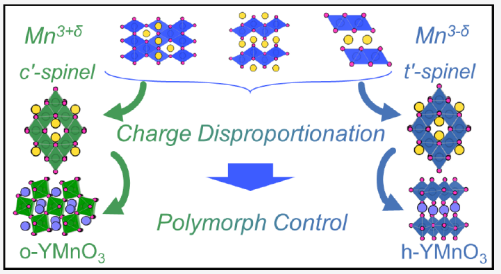

INTRODUCTION

In molecular chemistry, the understanding of precursor structure and composition permits product selectivity under mild reaction conditions. In comparison, product selectivity in inorganic materials synthesis is often limited to the product at a global or deep local minimum on a potential energy landscape due to the large thermal energy barrier of diffusion.[1] For more kinetic variables to influence the pathway, like the effect of precursor *structure* on product selectivity, the reaction must proceed to completion at low temperatures.[2]

A good starting point when synthesizing extended crystalline solids at low temperatures is to use a structural framework that retains geometric motifs from precursor to product. Specific examples include intercalation/deintercalation of cations or anions from a rigid inorganic framework.[3,4] Here, the precursor structure of a material determines the outcome of the reaction, such as achieving high capacities when cycling battery electrodes,[5] or selective replacement of interstitial cations in layered polymorphs of $LiAlO_2$.[6] Those topotactic examples are limited to the removal of labile ions from a rigid host structure, whereas most inorganic materials synthesis involves more complex reaction pathways where the structural similarities between precursor and product are less clear.

Solid-state metathesis provides a low-temperature route to crystalline materials where precursor composition and preparation can influence product selectivity.[7,8] In the preparation of complex oxides, we have shown that assisted metathesis reactions of the form $3A_2CO_3 + 2YCl_3 + Mn_2O_3 \xrightarrow{O_2} 2YMnO_3 + 6ACl + 3CO_2$ (A = Li, Na, K) selectively synthesized three unique yttrium manganese oxide products depending on the identity of the alkali carbonate precursor.[9] When using lithium, we identified $LiMnO_2$ and YOCl as intermediates that kinetically yield orthorhombic $YMnO_3$ at temperatures below 850 °C, rather than hexagonal $YMnO_3$ produced from reactions of the binary oxides at temperatures above 900 °C. By starting with these ternary materials as precursors, metathesis reactions can be performed directly

$$LiMnO_2 + YOCl \rightarrow LiCl + YMnO_3 \quad (1)$$

Received: July 8, 2020
Published: August 31, 2020

https://dx.doi.org/10.1021/acs.inorgchem.0c02023
Inorg. Chem. 2020, 59, 13639−13650

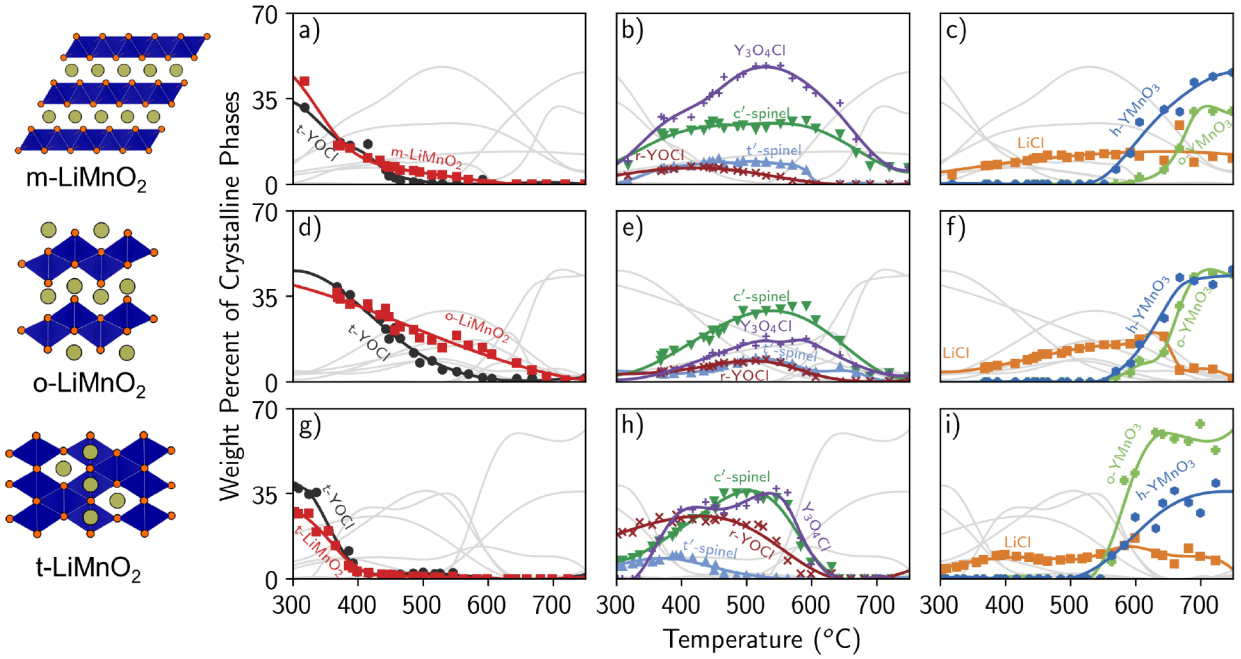

Figure 1. Refined weight fractions of crystalline materials at different reaction temperatures reveal the reaction pathway of the ternary metathesis reaction, $LiMnO_2$ + YOCl → LiCl + $YMnO_3$, when changing the $LiMnO_2$ precursor. Samples were heated for 40 min at the given temperature before being cooled to room temperature over the course of 30 min for an *ex post facto* measurement. Slow cooling was required to preserve the integrity of the LiCl weakened capillaries. Each row highlights the structure of the $LiMnO_2$ precursor and the reaction pathway as a function of temperature: (a−c) m-$LiMnO_2$ ($C2/m$), (d−f) o-$LiMnO_2$ ($Pmnm$), and (g−i) t-$LiMnO_2$ ($I4_1/amd$). Each column shows the phase fractions (weight percent) of crystalline phases present along the pathway. For clarity, the presented phases are separated into the reactants, $LiMnO_2$ (red square) and t-YOCl (black circle) (a,d,g); the intermediates, Y_3O_4Cl (purple cross), r-YOCl (rose x), t′-spinel (green triangle), and c′-spinel (sky blue triangle) (b,e,h); and the products, LiCl (orange square), h-$YMnO_3$ (blue hexagon), and o-$YMnO_3$ (light green cross) (c,f,i). Lines are provided to guide the eye.

to yield o-$YMnO_3$ at temperatures as low as 500 °C. This contribution expands on these ternary metathesis reactions by analyzing the effect of changing the $LiMnO_2$ precursor structure on the resulting reaction pathway.

The three polymorphs of $LiMnO_2$ crystallize as derivatives of the rock salt structure with octahedrally coordinated cation sites (Figure 1); however, the transition metal polyhedral connectivity varies between the structures. The monoclinic polymorph ($C2/m$, m-$LiMnO_2$) forms as a slightly distorted analog to $R\bar{3}m$ $LiCoO_2$, where the Jahn−Teller active Mn(III) induces a slight shift in the manganese oxide layering. m-$LiMnO_2$ is the most disordered of the three, with 10% of lithium sitting on manganese sites and vice versa.[10] The orthorhombic polymorph ($Pmnm$, o-$LiMnO_2$) is also a layered structure where the manganese oxide layers adopt a corrugated rock salt layering as compared to m-$LiMnO_2$. o-$LiMnO_2$ also has somewhat less site mixing, with only 5% cation inversion.[11] The tetragonal polymorph ($I4_1/amd$, t-$LiMnO_2$) orders with manganese sites forming the octahedral framework of a spinel and lithium occupying the remainder of the octahedral sites.[12] As this phase is formed by chemical insertion of Li into $LiMn_2O_4$ under mild conditions, it does not exhibit any notable site mixing in its pristine form.

Using *in situ* and recovered (*ex post facto*) temperature-dependent synchrotron X-ray diffraction (SXRD) along with neutron powder diffraction (NPD) data, we identify reaction intermediates and compare the temperature ranges by which they react to form $YMnO_3$ products. We discover that each reaction pathway when starting with different $LiMnO_2$ polymorphs proceeds through a series of defect accommodating intermediates: r-YOCl, Y_3O_4Cl, and two lithium manganese oxide spinels. The spinel intermediates form from a disproportionation reaction resulting in a reduced Mn(II,III) spinel resembling Mn_3O_4 and an oxidized Mn(III,IV) spinel resembling $LiMn_2O_4$. The relative amount of these two spinels changes as a function of reaction progress (e.g., how much LiCl had formed) and influences the amount of h-$YMnO_3$ and o-$YMnO_3$ that is observed after heating at ∼600 °C for 1 h. Density functional theory (DFT) based calculations reveal that o-$YMnO_3$ is stabilized through small concentrations of cation defects on the order of ∼2.2% in our observed products, which we correlate to the amount of oxidized Mn(III,IV) spinel present at the temperature when $YMnO_3$ forms. After 2 weeks of heating, these ternary metathesis reactions yield the slightly cation deficient o-$YMnO_3$. Controlling the composition and subsequent oxidation state of manganese in these spinel intermediates affords opportunities for increased kinetic control in the synthesis of complex oxides at low temperatures.

METHODS

Precursor Synthesis. YOCl was synthesized by heating yttrium chloride hexahydrate (Acros Organics, 99.9%) in an alumina crucible in air at 400 °C for 4 h with heating and cooling rates of 5 °C/min.[13]

$LiMn_2O_4$ was synthesized by reacting stoichiometric amounts of Li_2CO_3 (Baker, 99.3%) and Mn_2O_3. Mn_2O_3 was synthesized by heating $MnCO_3$ (Sigma-Aldrich, 99.9%) in an alumina crucible in air at 850 °C for 12 h with heating and cooling rates of 10 °C/min. The Li_2CO_3 and Mn_2O_3 powders were mixed using a mortar and pestle and heated in an alumina crucible at 800 °C for 24 h with heating and cooling rates of 10 °C/min. To prepare t-$LiMnO_2$, $LiMn_2O_4$ powder was refluxed under nitrogen in a 4 M acetonitrile solution with LiI (Alfa Aesar, 99.9%) where the overall Li:Mn ratio was 6:1.[14,15] The reflux was performed at 82 °C using an oil bath to maintain the

https://dx.doi.org/10.1021/acs.inorgchem.0c02023
Inorg. Chem. 2020, 59, 13639−13650

correct temperature. After refluxing, the powder was filtered and washed with acetonitrile to remove LiI and I_2 and dried under vacuum at 80 °C.

m-$LiMnO_2$ was synthesized by ion exchange from $NaMnO_2$.[16] $NaMnO_2$ was synthesized by reacting stoichiometric amounts of Na_2CO_3 (Macron Chemicals, 99.5%) and MnO_2 (Trinox 95%). The powders were mixed using a mortar and pestle and heated in an alumina crucible to 700 °C for 24 h with heating and cooling rates of 5 °C/min. The resulting black powder was moved into a glovebox antechamber while hot to prevent corrosion due to ambient humidity. $NaMnO_2$ was mixed with 3 times the stoichiometric amount of LiI using a mortar and pestle inside an Ar-filled glovebox. The mixture was heated to 460 °C for 4 h in an alumina crucible inside a sealed quartz ampule. The reaction was cooled for 9 h (1 °C/min). Excess LiI and NaI were removed by washing with water.

o-$LiMnO_2$ was synthesized by reacting Li_2CO_3 (Baker, 99.3%) and MnO_2 (Alfa Aesar, 99.9%) with 15 mol % excess Li_2CO_3. The powders were milled using an 8000 M Spex MixerMill within a 30 mL polypropylene bottle placed inside the steel Spex jar. The powders were milled for 90 min with 5 mm spherical yttria-stabilized zirconia milling media in a 2:1 weight ratio of media to sample. The resulting gray powder was pelleted using ∼1 short ton of force. The pellets were placed inside beds of sacrificial powder in an alumina boat and heated under flowing argon. The samples were heated at 600 °C for 4 h and 900 °C for 48 h with heating and cooling rates of 10 °C/min.

***Ex Situ* Reactions.** *Ex situ* control reactions were prepared by mixing $LiMnO_2$ and YOCl in a mortar and pestle for 15 min under argon. This homogenized mixture was pelleted using ∼1 short ton of force, placed in a cylindrical alumina crucible, and sealed in an evacuated quartz ampule (≤15 mTorr). Reactions were heated at 10 °C/min to the dwell temperature (500−600 °C). To avoid exposure to ambient oxygen due to the propensity for lithium chloride to chemically react with quartz at temperatures above 600 °C, long duration reaction ampules were placed into a larger diameter evacuated quartz ampule (e.g., double-sealed). Sample purity and product identification were verified by laboratory powder X-ray diffraction (PXRD) data collected on a Bruker D8 Discover diffractometer using Cu Kα radiation and a Lynxeye XE-T position-sensitive detector.

***Ex Post Facto* SXRD Reactions.** Synchrotron X-ray diffraction (SXRD) data were collected at beamline 28-ID-2 at the National Synchrotron Light Source II at Brookhaven National Laboratory. Data for all reactions were obtained using a gradient furnace, where the calibrated horizontal beam position defines the sample temperature.[17] In the gradient furnace, varying densities of heating elements along the device allow for a single capillary to be simultaneously heated to a range of temperatures as a function of position along the capillary. Samples were loaded into a 1.1 mm OD quartz capillary and sealed with epoxy (Aremco-Bond 570). Calibration of detector curvature was performed using CeO_2 at all points along the gradient furnace using pyFAI.[18] A single characteristic position was set to 450 °C (using a PID-controlled power source) which created a reproducible temperature range from 300 to 750 °C along the capillary. Position was related to temperature with a calibration run based on the thermal expansion of NaCl.[19] Samples were held at temperature for 40 min before being cooled over the course of 35 min to room temperature. Slow cooling was necessary to prevent the capillary from breaking after it had been exposed to LiCl at high temperatures. *Ex post facto* diffraction patterns were then taken along the length of the capillary with a wavelength of 0.1949 Å for m-$LiMnO_2$ and o-$LiMnO_2$ and 0.19319 Å for t-$LiMnO_2$. SXRD data were collected on a PerkinElmer plate detector at a distance of 1400 mm. The experimental data was reduced in real-time using analysis software xpdAn and xpdTools that are open source projects in the xpdAcq organization on GitHub (https://github.com/xpdAcq).

***In Situ* NPD Reactions.** Neutron powder diffraction (NPD) experiments were performed at beamline BL-11A POWGEN at the Spallation Neutron Source at Oak Ridge National Laboratory. The samples were measured using the MICAS vacuum furnace with the AGES gas handling insert.[20] Stoichiometric mixtures of $LiMnO_2$ and YOCl were mixed with an agate mortar and pestle in an argon-filled glovebox. Then, the homogenized powder was loaded into quartz baskets lined with Al_2O_3 cloth (Zircar Zirconia, Tricon Knit Cloth). The Al_2O_3 cloth was used to minimize Li-containing compounds from reacting with the quartz holder. For *in situ* measurements, the samples were heated in argon at a rate of 1 °C/min, and 1 h dwell scans were collected every 50 °C starting at 100 °C for the t-$LiMnO_2$ mixture and 250 °C for the o-$LiMnO_2$ and m-$LiMnO_2$ mixtures. The t-$LiMnO_2$ mixture was kept below the melting point of LiCl, reaching a maximum temperature of 500 °C to prevent leakage of molten LiCl through the glass frit holding up the sample. The glass baskets were redesigned with a closed bottom for subsequent experiments with m-$LiMnO_2$ and o-$LiMnO_2$ to access higher temperature and observe the formation of $YMnO_3$. NPD patterns of empty quartz baskets lined with Al_2O_3 cloth were collected every 100 °C and were subtracted from the *in situ* diffraction patterns.

***In Situ* SXRD Reactions.** *In situ* SXRD experiments were performed at beamline 17-BM-B (λ = 0.2415 Å) at the Advanced Photon Source (APS) at Argonne National Laboratory using a PerkinElmer plate detector at a distance of 700 mm. Homogenized metathesis precursors were packed into a quartz capillary (1.1 mm OD, 0.9 mm ID) at CSU in an argon-filled glovebox. Then, capillaries were sealed under vacuum (<20 mTorr) using a methane-oxygen torch. All capillaries were loaded into a flow-cell apparatus[21] equipped with resistive heating elements and heated at 10 °C/min to 600 °C. While heating, the samples were continuously rocked at ±5° around the axis of the capillary. Diffraction patterns were collected every 2 s and summed every 20 s. Images collected from the plate detector were integrated using GSAS-II and calibrated using a LaB_6 standard.

Rietveld Refinements. Quantitative phase analysis of X-ray and neutron data diffraction data was performed using the Rietveld method as implemented in TOPAS v6. To consistently analyze powder patterns which could contain upward of five distinct crystallographic phases, the following assumptions were made for analyzing X-ray diffraction data: atomic displacement parameters (ADPs) were fixed using a B_{iso} value of 2.5 Å^2 for all atoms, peak broadening was assumed to be a result of crystal size using a Lorentzian function, and site occupancies were fixed at one. Lattice parameters were held constant when the calculated weight percents were less than 5% due to the large amount of overlap between intermediate phases in the diffraction data. For analyzing weight percents in neutron diffraction data, the ADPs were refined, peak broadening was fit as a function of Lorentzian and Gaussian functions, and all site occupancies were fixed at full occupancy of 1. To obtain occupancies from neutron diffraction data, the ADPs were fixed at 1.5 Å^2, and the occupancies were refined. Data from post ex facto SXRD runs is plotted as weight percent to account for inconsistent packing densities along the length of the capillary. The data should be considered qualitative as a result.

Computational Methods. Theoretical calculations were performed to evaluate the thermodynamic stability of $YMnO_3$ polymorphs using density functional theory (DFT) as implemented in the Vienna *Ab initio* Simulation Package (VASP).[22] We used the Generalized Gradient Approximation (GGA) with the Perdew−Burke−Ernzerhof (PBE) exchange-correlation functional[23] plus the Hubbard-*U* extension (GGA + *U*) with *U* = 3.9 eV for Mn.[24,25] The Projector Augmented Wave (PAW) method[26,27] was used for modeling core states with a plane wave basis and an energy cutoff of 520 eV. The Python Materials Genomics package (*pymatgen*)[28] was used to create and process all VASP input/output files. The *phonopy*[29] package was used to process force constants, apply the quasiharmonic approximation (QHA), and produce the Gibbs free energy, $G(T, P)$, of each structure.

The original structures for the hexagonal[30,31] and orthorhombic[32] $YMnO_3$ polymorphs were acquired from the Materials Project database.[33] Initial calculations showed that the calculated material properties were particularly sensitive to the initialized magnetic ordering of the structures. For example, all structural relaxations performed using the GGA+*U* scheme with a ferromagnetic (FM) ordering yield an incorrect zero band gap for both the

https://dx.doi.org/10.1021/acs.inorgchem.0c02023
Inorg. Chem. 2020, 59, 13639−13650

centrosymmetric (high-temperature) and noncentrosymmetric (low-temperature) h-$YMnO_3$ structures. Previous studies suggest that below their Néel temperatures, the hexagonal and orthorhombic phases acquire triangular and sinusoidally modulated antiferromagnetic (AFM) orderings, respectively.[34,35] To initialize an appropriate magnetic ordering in our calculations, we enumerated many possible collinear magnetic orderings for each structure using the high-throughput DFT workflow developed by Horton et al.[36] We found several orderings which opened the GGA-calculated band gap to 1−2 eV for both the hexagonal and orthorhombic phases. Each of these collinear orderings was of AFM type and slightly higher in energy (<2 meV/atom) than any of the FM orderings. For each structure, we selected the lowest energy AFM ordering which also resulted in a substantial nonzero band gap. The original MP structures were then rerelaxed with these AFM orderings in 2 × 2 × 2 supercells with a *k*-point grid density of 5000/atom until forces on the atoms were 1×10^{-4} eV/Å or less.

Density functional perturbation theory (DFPT) was used to calculate force constants for 11 equally spaced deformations spanning ±4% lattice strain of the rerelaxed (primitive) cells. We used a *k*-point grid density of 5000/atom, plane wave energy cutoff of 620 eV, and energy convergence criterion of 1×10^{-8} eV for the self-consistent electronic loop. Force constants were mass-weighted and symmetrized to acquire phonon modes used to approximate the Helmholtz free energy, $F(T, V)$, as a function of volume of the deformed cells. Using *phonopy*, the Vinet equation of state[37] was fit to these free energy curves for each structure at temperatures ranging from $T = 0$ to 1400 K (in 100 K steps) and minimized at a pressure of $P = 1$ atm, yielding the Gibbs free energy curves, $G(T, P)$, of each structure.

Vacancy formation energies for yttrium and manganese cations, $E^f[V_Y]$ and $E^f[V_{Mn}]$, were calculated for each $YMnO_3$ structure via the charged-defect supercell approach with finite-size corrections developed by Freysoldt et al.[38,39] and implemented by Broberg et al.[40] in the *atomate* workflow interface.[41] We used a *k*-point grid density of 100/atom and supercell dimensions outlined in Table S12. Using computed defect formation energies, the thermodynamic stability of the polymorphs was modeled using a defect concentration-dependent thermodynamic potential, Φ, defined as

$$\Phi(T, P, x) = G^{\mathrm{QHA}}(T, P) + (E^f[V_Y] + E^f[V_{Mn}])x \quad (2)$$

where T is the temperature, P is the pressure, $G^{\mathrm{QHA}}(T, P)$ is the Gibbs free energy calculated using QHA, $E^f[V_Y]$ and $E^f[V_{Mn}]$ are the defect formation energies of yttrium and manganese vacancies, respectively, and x is the concentration of cation vacancies in $Y_{1-x}Mn_{1-x}O_3$. A paired cation vacancy concentration was used as an equivalent representation of oxygen hyperstoichiometry $YMnO_{3+\delta}$, where $x = \delta/(3 + \delta)$. This aligns with previous observations that rare-earth perovskite manganites $RMnO_3$ accommodate excess oxygen via cation (R, Mn) vacancies (instead of oxygen interstitials) due to their close-packed structure.[42−45] It was noted that in $LaMnO_3$, cation vacancies were found in equal proportions for small values of δ,[43] although this is not necessarily true for more oxidizing conditions.[44]

Entropic contributions to vacancy formation were not included in the calculation of vacancy formation energies. Thus, the calculated vacancy formation energies, $E^f[V_Y] + E^f[V_{Mn}]$, are independent of temperature. The Fermi energy of electrons, E_F, which is typically solved for self-consistently via charge balance of defect concentrations at equilibrium, was left as a free variable in phase diagram construction.

RESULTS

The reaction of $LiMnO_2$ and YOCl to form $YMnO_3$ and LiCl through defect accommodating intermediates can be generally described as

$$\mathrm{LiMnO_2} + \mathrm{YOCl} \rightarrow \epsilon\mathrm{LiCl} + \mathrm{Li_{1-\epsilon}MnO_{2-\epsilon/2}} + \mathrm{YO_{1+\epsilon/2}Cl_{1-\epsilon}} \rightarrow \mathrm{LiCl} + \mathrm{YMnO_3} \quad (3)$$

where ϵ describes the amount of lithium chloride that has formed at a particular temperature or time, and $Li_{1-\epsilon}MnO_{2-\epsilon/2}$ and $YO_{1+\epsilon/2}Cl_{1-\epsilon}$ describe the average composition of two disproportionated lithium manganese oxide spinels and two oxygen-rich yttrium oxychloride intermediates (r-YOCl, Y_3O_4Cl), respectively. As the value of ϵ changes over the progress of the reaction, we observe different crystalline intermediates that describe these average compositions. The composition of these intermediates defines the reaction pathway and therefore the distribution of the final $YMnO_3$ products.

Thermodiffraction using synchrotron and neutron radiation reveals the influences of the precursor polymorph on this reaction. Synchrotron X-ray diffraction (SXRD) experiments were performed on a gradient furnace, which heats a single capillary to a range of temperatures along the length of the sample, with the coolest part of the sample at 300 °C and the hottest part at 750 °C. After being heated for 40 min, the sample was cooled. Diffraction patterns were then taken at room temperature after heating, defined here as *ex post facto* or "after the fact" SXRD. This technique allows one to directly compare lattice parameters between phases formed at different dwell temperatures without needing to consider thermal expansion. Using the gradient furnace also permits the collection of isothermal *in situ* kinetic data. The quantitative analysis of crystalline phases from *ex post facto* SXRD experiments is shown in Figure 1 with temperature values reported in Tables S1−S3, and reactive temperature ranges of each phase illustrated in Figure S2. Complementary temperature-dependent neutron powder diffraction (NPD) experiments were also performed to confirm the identity of observed intermediates and to better analyze the composition of lithium-containing intermediates. The quantitative phase analysis from NPD experiments is shown in Figure S3, and details about formation of the phases are provided in Tables S4−S6.

Regardless of the $LiMnO_2$ precursor, the first observed reaction forms lithium chloride, two manganese-containing spinel phases, and oxygen-rich yttrium oxide chloride (Figures 1 and S3). The two spinel intermediates formed as lithium and oxygen are removed from $LiMnO_2$ to form LiCl and Y_3O_4Cl, respectively. Here, a disproportionation of $LiMnO_2$ into two distinct spinel phases is observed: a cubic spinel phase resembling $Fd\bar{3}m$ $LiMn_2O_4$ (c′-spinel) and a tetragonal spinel phase resembling $I4_1/amd$ Mn_3O_4 (t′-spinel). In SXRD experiments collected *ex post facto* (Figure 1), the relative weight percent of the c′-spinel is at least double that of the t′-spinel for all reaction pathways, yet *in situ* SXRD and NPD experiments yield more t′-spinel over similar temperature ranges (Figures S1 and S3). Concomitantly, *Cmcm* Y_3O_4Cl forms through the oxygenation of the t-YOCl precursor. This reaction proceeds through a disordered rhombohedral form of YOCl ($R\bar{3}m$) that is poorly resolved in the diffraction data but has been previously observed in assisted metathesis reactions with lithium.[46] The results in Figure 1b,e,h confirm the presence of each intermediate, yet subtle differences are observed in the precursor reactivity, the relative amounts of each intermediate, and the temperature range over which the intermediates form and react.

The reaction pathway starting with m-$LiMnO_2$ (Figure 1a−c) yields intermediates at the lowest temperatures when compared to the other polymorphs of $LiMnO_2$, yet the intermediates do not react fully until temperatures reach 600 °C. In Figure 1b, significant amounts of r-YOCl, Y_3O_4Cl, the

https://dx.doi.org/10.1021/acs.inorgchem.0c02023
Inorg. Chem. 2020, 59, 13639−13650

two manganese-containing spinel phases, and LiCl form by 300 °C. *In situ* SXRD experiments in Figure S1 confirm that the relative amounts of each precursor begin decreasing at temperatures as low as 150 °C to yield c′-spinel and r-YOCl. Furthermore, calculated site occupancies from the *in situ* NPD experiments reveal the occupancy of the (2d) lithium site of m-$LiMnO_2$ in Figure 2 decreases by ∼24% by 300 °C, whereas

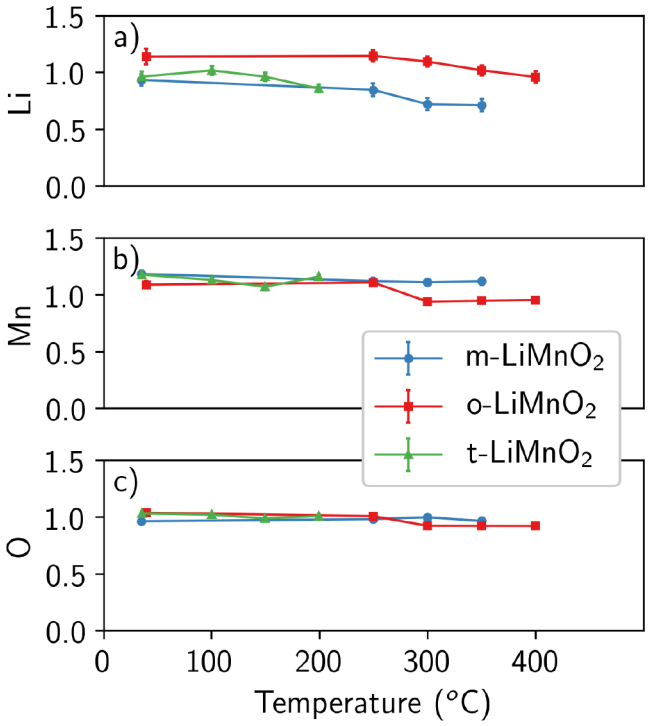

Figure 2. Occupancy of crystallographic sites that correspond to lithium-rich (left), manganese-rich (center), and oxygen (right) sites within the crystal lattice for the o-$LiMnO_2$ (red), m-$LiMnO_2$ (blue), and t-$LiMnO_2$ (green). As all occupancies were refined together with the scale factor for the phase, values should be considered relative rather than absolute.

the oxygen occupancy remains constant. The m-$LiMnO_2$ and YOCl precursors continue to react until depleted at 570 and 443 °C, respectively. Near 500 °C, the relative amount of the reaction intermediates is the highest, with Y_3O_4Cl representing the largest fraction at 48 wt %. Here, the intermediates react to yield different polymorphs of $YMnO_3$. First, r-YOCl and t′-spinel react at lower temperatures (r-YOCl: 465 °C; t′-spinel: 570 °C) followed by Y_3O_4Cl and c′-spinel (Y_3O_4Cl: 592 °C; c′-spinel: 644 °C). As all intermediates start to decrease, the h-$YMnO_3$ phase forms at 570 °C followed by the formation of o-$YMnO_3$ at 644 °C. More h-$YMnO_3$ is formed as a result of this reaction with 50% more h-$YMnO_3$ present at 750 °C. LiCl intensity in the SXRD *ex post facto* data decreases rapidly at 600 °C when starting with o-$LiMnO_2$. In its place, the capillary began to crystallize into a trigonal silicate phase, indicating that LiCl reacted with the reaction vessel. The silicate phase is modeled using the LeBail method and is not accounted for in the wt % of the final product presented in Figure 1.

The reaction starting from o-$LiMnO_2$ (Figure 1d–f) yields a pathway where the precursors begin to react near 300 °C and persist to the highest observed temperatures (o-$LiMnO_2$: 668 °C; YOCl: 495 °C). Compared to m-$LiMnO_2$, o-$LiMnO_2$ begins reacting at higher temperatures, as supported in the calculated lithium site occupancies in Figure 2 and *in situ* NPD results in Figure S3. As precursors react, the same intermediates are formed; however, there is significantly less Y_3O_4Cl formed at a maximum of 18 wt % at 530 °C as compared to 48 wt % at the same temperature for reactions starting with m-$LiMnO_2$. Also, the t′-spinel intermediate is observed up to 606 °C. Here, a concomitant decrease of phase fraction for all intermediate phases is observed resulting in equal amounts of h-$YMnO_3$ and o-$YMnO_3$ formed at 570 and 606 °C, respectively.

For reactions starting with the t-$LiMnO_2$ polymorph, the precursors react over a narrower temperature range, where t-$LiMnO_2$ and YOCl are completely depleted by 392 °C in Figure 1g and m-$LiMnO_2$ and o-$LiMnO_2$ persist to higher temperatures of 570 and 668 °C respectively. This is evident in the calculated site occupancies in Figure 2, where the (4a) lithium site occupancy appears to decrease below 300 °C yet is completely reacted by 300 °C. Contrary to the other $LiMnO_2$ polymorphs, there is a significant fraction of t′-spinel compared to c′-spinel at 300 °C. This t′-spinel reacts at 400 °C to yield more c′-spinel in Figure 1h. Also, r-YOCl forms in a relatively large amount reaching 26 wt % as opposed to a maximum of 7 and 9 wt % for reactions with m-$LiMnO_2$ and o-$LiMnO_2$, respectively. Near 500 °C, Y_3O_4Cl, r-YOCl, and c′-spinel react completely by 560 °C to yield o-$YMnO_3$ and h-$YMnO_3$. Here, 25% more o-$YMnO_3$ was observed than h-$YMnO_3$ at 725 °C.

Central to understanding the reaction pathway in these ternary metathesis reactions is the disproportionation of spinel intermediates into a c′-spinel and t′-spinel (Figure 1 b,e,h). To properly identify the two phases, both SXRD and NPD are needed. In the SXRD results, this spinel disproportionation is most easily observed in diffraction patterns taken from the reaction o-$LiMnO_2$ + YOCl (Figure 3), as Bragg peaks from both the monoclinic and tetragonal polymorphs of $LiMnO_2$ overlap with those of the t′-spinel phase (Figure S4). The c′-spinel is most evident in the X-ray diffraction patterns (Figure 3a, Figure S4) by the strong (111) reflection at Q = 1.33 Å^{-1}. The t′-spinel is harder to distinguish with X-rays, as evidenced by the small $(112)_t$ peak at Q = 2.04 Å^{-1}, or by a small shoulder on the $(111)_c$ peak of c′-spinel corresponding to the $(101)_t$ peak at Q = 1.28 Å^{-1}. In the neutron diffraction pattern (t-$LiMnO_2$ + YOCl) presented in Figure 3b, the t′-spinel is easily identifiable by a strong (202) reflection at 2.55 Å^{-1}, and the c′-spinel is identified by the (202) reflection at 2.64 Å^{-1}. The site occupancies of the t′-spinel phase were refined from the neutron data and indicated the presence of lithium on the tetrahedral (4c) manganese site of Mn_3O_4, with a refined Li occupancy of 0.43 ± 0.15 at 450 °C. The intensity of Bragg peaks from the c′-spinel in NPD results is not high enough to successfully refine occupancies of this phase. While we are unable to refine the occupancies of all observed spinel intermediates and achieve a unique result, we simply note that site mixing on this tetrahedral site can occur.

Simultaneous formation of the cubic and tetragonal spinel phases (Figure 4) suggests a charge disproportionantion of manganese during the reaction. The tetragonal spinel unit cell is distinguishable crystallographically by a contraction of the a_t axis due to a Jahn–Teller distortion of Mn(III)-containing [MnO_6] octahedra. To ensure the validity of refining both cubic and tetragonal spinel phases, the c′-spinel was fit using a formally tetragonal setting ($I4_1/amd$ $LiMn_2O_4$) which refined to a metrically cubic unit cell when $a_t = b_t = \sqrt{2} \times c_t$ (e.g., the c_t/a_t ratio remained close to the expected value of 1.41 for a

https://dx.doi.org/10.1021/acs.inorgchem.0c02023
Inorg. Chem. 2020, 59, 13639–13650

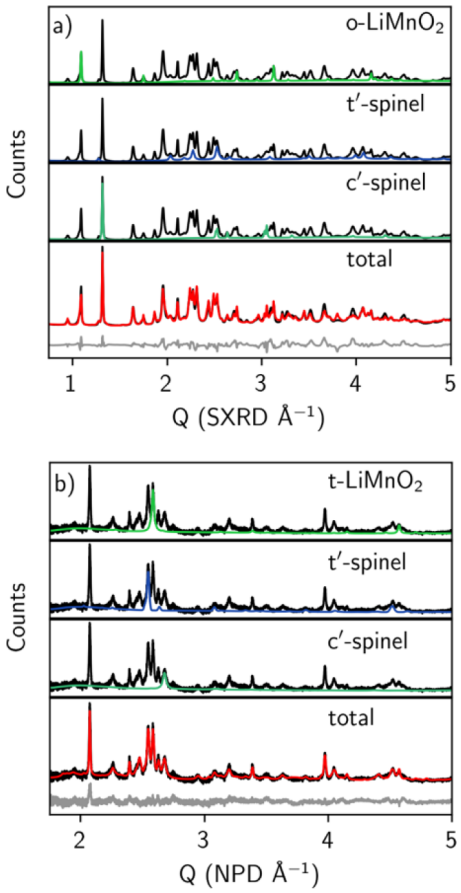

Figure 3. Diffraction patterns that illustrate the presence of two unique manganese-containing spinel intermediates in these ternary metathesis reactions: a) SXRD patterns of o-$LiMnO_2$ + YOCl at 500 °C and b) NPD patterns of t-$LiMnO_2$ + YOCl at 400 °C. The contributions of each lithium manganese oxide phase are highlighted: $LiMnO_2$ precursor (top), t′-spinel (second from top), and c′-spinel (third from top). The overall fit from Rietveld refinement (bottom) also contains t-YOCl, r-YOCl, Y_3O_4Cl, and LiCl (red) along with a difference pattern (gray).

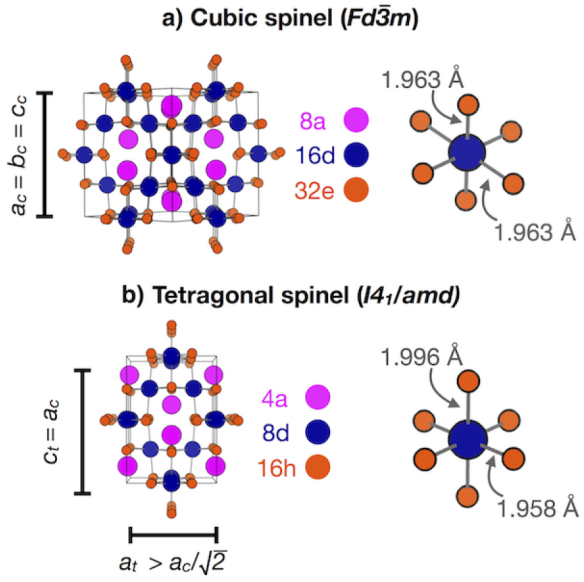

Figure 4. Structural relationship between a) cubic $Fd\bar{3}m$ spinel and b) tetragonal $I4_1/amd$ spinel. The geometric relationship between unit cells is shown by the Wyckoff positions highlighted. The tetrahedral cation sites ($(8c)_c$ and $(4c)_t$), octahedral cation sites ($(16d)_c$ and $(8c)_t$), and oxygen sites ($(32e)_c$ and $(16h)_t$) are highlighted. Finally, the local [MnO_6] octahedra are shown for each structure with the axial and equatorial bond distances labeled to highlight the Jahn–Teller distortion in tetragonal spinels

cubic spinel in Figure S5a). For comparison, the t′-spinel c_t/a_t ratio yielded a tetragonal ($I4_1/amd$) cell with a c_t/a_t ratio of 1.63 (Figure S5b). The suppression of a Jahn–Teller distortion in c′-spinel and the simultaneous presence of the distortion in t′-spinel suggests a charge disproportionation between the two intermediates.

Density functional theory calculations show that small changes in the manganese oxidation state can change the relative stability of the two $YMnO_3$ polymorphs. A previous study[47] showed that the orthorhombic polymorph o-$YMnO_3$ is readily produced and stabilized in oxygen-rich environments. As with other perovskite manganites, excess oxygen, δ, in o-$YMnO_{3+\delta}$, has been shown to manifest as the formation of nearly equivalent amount cation (yttrium and manganese) vacancies, x, in $Y_{1-x}Mn_{1-x}O_3$. It was hypothesized by Bergum et al. that excess oxygen stabilizes the orthorhombic phase via an increase in perovskite geometric stability resulting from the decrease in ionic radius that occurs with partial oxidation of Mn(III) to Mn(IV).[48] To computationally test this hypothesis, we first calculated the defect-free Gibbs free energies, $G(T, P)$, for the hexagonal and orthorhombic polymorphs using the QHA approach for considering phonon vibrational entropy contributions. We also considered the centrosymmetric hexagonal structure ($P6_3/mmc$), which through a ferroelectric phase transition is stable at temperatures above $T \sim 1250$ K.[49] In our calculations, we find that the typical ground-state hexagonal ($P6_3cm$) structure is thermodynamically stable at all temperatures considered, $T \leq 1400$ K, and a pressure of $P = 1$ atm. The orthorhombic ($Pnma$) polymorph and centrosymmetric hexagonal polymorph ($P6_3/mmc$) Gibbs free energies were approximately +23.0 and +19.9 meV/atom higher than that of the hexagonal phase at $T = 0$ K, decreasing to +7 and +11 meV/atom at $T = 1400$ K, respectively. The Gibbs free energies and heat capacities, $c_p(T)$, are shown as a function of temperature in Figure S6.

Calculations allow us to determine the cutoff threshold for o-$YMnO_3$ stability with respect to cation vacancies. The defect-dependent thermodynamic potential, $\Phi(T, P, x)$, given by eq 2, was minimized at $P = 1$ atm resulting in the phase diagram in Figure 5. The cation-deficient orthorhombic polymorph, o-$Y_{1-x}Mn_{1-x}O_3$, is predicted to be stable above a defect concentration threshold of approximately $x \simeq 0.022$ (2.2%) at $T = 0$ K, which appears to decrease with temperature. The centrosymmetric hexagonal structure h-$YMnO_3$ ($P6_3/mmc$) was not found to be the minimum energy phase of the three structures at any values of T or x and hence does not appear in the diagram. Figure S9 shows the sensitivity of this phase boundary to the value of Fermi energy, E_F. Lower values of E_F merely shift the location of the phase boundary toward slightly higher values, near $x \sim 0.034$ at $T = 0$ K. Furthermore, changes in the values of chemical potentials have no effect on the phase diagram (with the caveat that negative defect formation energies are unphysical) since the polymorphs are compared with *identical* compositions at all points on the diagram.

Importantly, and in agreement with the hypothesis by Bergum et al., the significantly lower cation vacancy formation energies in the orthorhombic phase offset the difference in

https://dx.doi.org/10.1021/acs.inorgchem.0c02023
Inorg. Chem. 2020, 59, 13639–13650

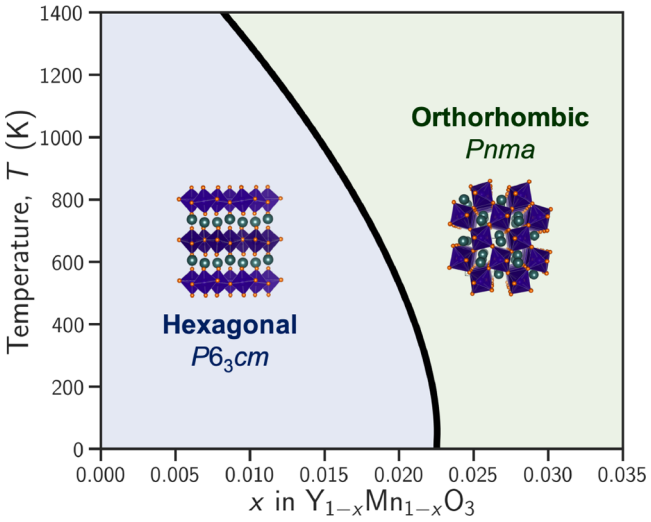

Figure 5. DFT-calculated phase diagram of cation-deficient $YMnO_3$ polymorphs with respect to temperature, T, and a fixed, equal concentration of cation (Y,Mn) vacancies, x, in $Y_{1-x}Mn_{1-x}O_3$. All structures are initialized with AFM magnetic orderings, and the Fermi energy of electrons is fixed at E_F = 1.0 eV.

energies due to polymorphism (~20 meV/atom) between the hexagonal ($P6_3cm$) and orthorhombic structures. According to the defect formation energy curves, which are shown in Figure S8, o-$YMnO_3$ exhibits significantly lower cation vacancy formation energies than h-$YMnO_3$ ($P6_3cm$). This difference, of 2.5 and 2.6 eV for Y and Mn vacancies, respectively, at E_F = 1.0 eV, appears to stabilize the orthorhombic phase even at very small cation vacancy concentrations, on the order of ~2–3%. These vacancies correspond to an increased oxidation state of manganese in order to maintain charge neutrality in the structure.

While the reaction pathway can control the initial polymorph selectivity of $YMnO_3$, over long periods of time the defects can equilibrate to lead to a single $YMnO_3$ product. Control reactions were performed at 550 °C, for each $LiMnO_2$ precursor, to determine product selectivity in these ternary metathesis reactions. Figure 6 depicts the phase fractions from PXRD results after short (1 h) and long (168 or 336 h) duration reactions. After dwelling for 1 h at 550 °C, reactions starting with m-$LiMnO_2$ yield the highest conversion to products, which supports the lower onset temperature for $YMnO_3$ in Figure 1c. Interestingly, o-$YMnO_3$ is observed as the majority phase over h-$YMnO_3$ after 1 h (Figure 6a). Both t-$LiMnO_2$ and o-$LiMnO_2$ reactions yield little conversion to $YMnO_3$ after 1 h, which also supports the results in Figure 1f and i, where 550 °C was near the onset temperature of $YMnO_3$ for both reactions. After long duration reactions with m-$LiMnO_2$, o-$YMnO_3$ is the only product observed, whereas o-$LiMnO_2$ and t-$LiMnO_2$ yield mixtures of hexagonal and orthorhombic $YMnO_3$ after 1 week at 550 °C suggesting these reactions are not at equilibrium after 1 week.

As reactions starting with m-$LiMnO_2$ yield $YMnO_3$ products at the lowest temperatures and reaction times, control reactions performed at varied reaction temperatures yield a better understanding of how $YMnO_3$ phase selectivity changes with reaction temperature. Figure 7a–c shows the product distribution calculated from Rietveld refinements of laboratory PXRD data at different reaction temperatures (500–600 °C) as a function of time of reaction (without remixing). Taken

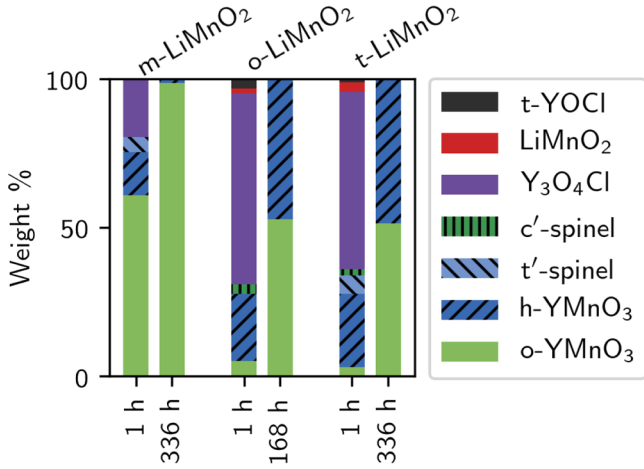

Figure 6. Refined fraction of reaction products taken from laboratory PXRD data of *ex situ* ternary metathesis reactions ($LiMnO_2$ + YOCl) at 550 °C comparing short and long duration reactions. The results are separated by the $LiMnO_2$ precursor: a) monoclinic ($C2/m$), b) orthorhombic ($Pmnm$), and c) tetragonal ($I4_1/amd$).

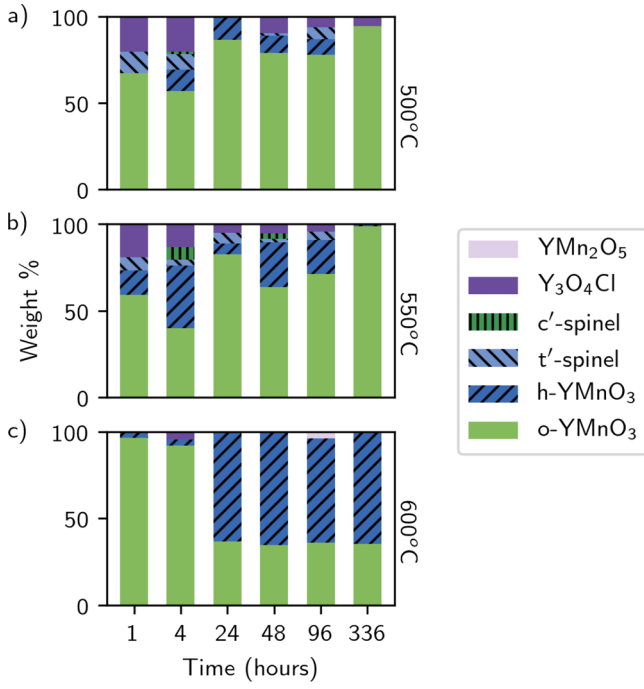

Figure 7. Refined fraction of reaction products taken from laboratory PXRD data of *ex situ* ternary metathesis reactions ($LiMnO_2$ + YOCl) at varied temperatures and reaction times. Subplots (a–c) show the progression of reaction products when starting with monoclinic ($C2/m$) m-$LiMnO_2$ at (a) 500 °C, (b) 550 °C, and (c) 600 °C. As the temperature increases, the hexagonal $YMnO_3$ product selectivity increases over the orthorhombic product.

together, the results from these *ex situ* reactions reveal a change in phase selectivity of $YMnO_3$ products as a function of temperature. Below 600 °C, the orthorhombic phase dominates after long duration reactions. At 600 °C or above, the product fraction shifts to favor h-$YMnO_3$ at longer time point reactions, but a mixture of polymorphs still exists after 2 weeks at 600 °C.

https://dx.doi.org/10.1021/acs.inorgchem.0c02023
Inorg. Chem. 2020, 59, 13639–13650

DISCUSSION

Reaction Pathway. The reaction of $LiMnO_2$ and YOCl to form LiCl and $YMnO_3$ proceeds through a number of crystalline intermediates which can be observed in diffraction experiments. The two yttrium-containing intermediates (r-YOCl and Y_3O_4Cl) show to what extent the reaction has progressed (ϵ in eq 3), while the two manganese-containing intermediates (c′-spinel and t′-spinel) control the ratio of hexagonal and orthorhombic $YMnO_3$ formed in the final product (Figure 8). By understanding the pathway, insight and control over the reaction can be obtained.

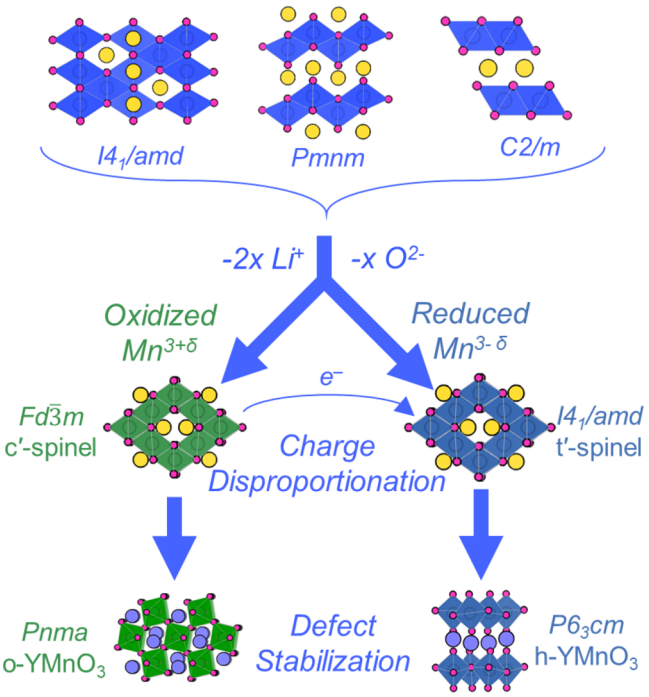

Figure 8. Structure of reactants, proposed intermediates, and products along the metathesis pathway. The charge disproportionation to form c′-spinel and t′-spinel stabilizes o-$YMnO_3$ and h-$YMnO_3$, respectively.

As the reaction progresses, the yttrium oxychloride precursor loses chlorine to LiCl and replaces it with oxygen obtained from lithium manganese oxide species in the reaction. The intermediate $YO_{1+\epsilon/2}Cl_{1-\epsilon}$ crystallizes into two distinct phases. At low values of ϵ, the more chlorine-rich rhombohedral r-YOCl forms. As more chlorine in the structure is replaced with oxygen, an orthorhombic Y_3O_4Cl type phase forms with the composition $YO_{1+\epsilon/2}Cl_{1-\epsilon}$ with a maximum ϵ of 2/3. Beyond ϵ = 2/3, we hypothesize Y_2O_3 will form, yet we do not observe this phase as an intermediate. Previous studies have observed the transition $Y_3O_4Cl \rightarrow Y_2O_3$ in related metathesis reactions,[46] as well as in thermogravimetric studies of rare-earth halides.[13,50] In those studies, oxygenation occurred when performing the reactions in air or under flowing oxygen. In a sealed environment, as studied here, oxygen must come from the reaction to yield lithium manganese oxide spinels. Further chlorine loss and oxygen abstraction from lithium manganese oxide phases past the point of ϵ = 2/3 requires conversion to an oxide.

In eq 3, the Li−Mn−O intermediates are represented generally as $Li_{1-\epsilon}MnO_{2-\epsilon/2}$, yet we observe two distinct spinel intermediates: a c′-spinel resembling cubic $Fd\bar{3}m$ $LiMn_2O_4$ and a t′-spinel resembling tetragonal $I4_1/amd$ Mn_3O_4. Here, the two spinel intermediates formed from a disproportionation reaction as lithium and oxygen leave the phase to form LiCl and oxygenated $YO_{1+\epsilon/2}Cl_{1-\epsilon}$. The observation of two spinels can be attributed to the well-known propensity of Jahn−Teller active Mn(III) to distort the $[MnO_6]$ octahedra in these spinels, as presented in Figure 4. This disproportionation can manifest in different ways in these Li−Mn−O spinels as a function of composition and oxidation state of manganese. The effect of losing either oxygen or lithium from $LiMnO_2$ has been previously investigated in the context of lithium ion batteries. With all Mn(III), $Li_2Mn_2O_4$ adopts the tetragonal $I4_1/amd$ spinel structure, where all $[MnO_6]$ are distorted. Upon delithiation, a phase transition to the cubic spinel, $Fd\bar{3}m$ $LiMn_2O_4$, is observed. This cubic spinel is observed electrochemically over the range $0.24 < Li_xMn_2O_4 < 1$, or when the manganese oxidation state is greater than 3.5.[51] When x = 0.24, a disproportionation reaction occurs, resulting in a Mn(IV) cubic spinel ($Li_4Mn_5O_{12}$) and a mixed Mn(II,III) tetragonal spinel (Mn_3O_4).[52] Alternatively, the presence of oxygen vacancies in the cubic spinel $LiMn_2O_{4-\delta}$ also results in a similar disproportionation. Here, the cubic spinel is observed when $(4-\delta) > 3.833$. Then, a disproportionation reaction occurs to yield tetragonal Mn_3O_4, cubic $LiMn_2O_{4-\delta}$, and tetragonal $Li_2Mn_2O_4$ over the range $3.33 < (4-\delta) < 3.833$.[53]

The disproportionation reaction in the ternary metathesis reactions studied here differs from those cases, as both lithium and oxygen vacancies are introduced simultaneously. Therefore, we define a range in manganese oxidation states for cubic spinels, +3.33 < Mn < +3.88, where the end points represent $LiMn_2O_{3.833}$ and $Li_{0.24}Mn_2O_4$, respectively. Then, we apply these constraints to describe the observed disproportionation reaction into c′-spinel and t′-spinel intermediates

$$Li_{1-\epsilon}MnO_{2-\epsilon/2} \rightarrow y(t'\text{-}Li_xMn_{3-x}O_{4+z}) + c'\text{-}Li_{1-\epsilon-yx}Mn_{1-3y+yx}O_{2-\epsilon/2-4y-zy} \quad (4)$$

where x is the degree of site mixing on the tetrahedral site of the t′ spinel, and y represents the amount of t′ spinel relative to c′ spinel upon disproportionation. The variable z determines the amount of cation vacancies in t′-spinel, which is related to the extent of charge disproportionation of Mn(III) to Mn(II) and Mn(IV). In eq 4, we assume some concentration of lithium on the tetrahedral site of the t′ spinel, as evidenced from neutron diffraction data; yet, the disproportionation reaction could plausibly yield Mn_3O_4 when x = 0. As constructed, the composition of these spinels can exist up to x = 0.5. At x = 0.5, the t′-spinel would formally be $Li_{0.5}Mn_{0.5}Mn_2O_4$ where the oxidation state of manganese would remain Mn(III), thus making disproportionation redundant. The value of y in eq 4 then becomes directly influenced by the amount of lithium on the tetrahedral site of the t′-spinel. Lower values of x will result in more t′-spinel Mn_3O_4 with Mn(II,III), whereas higher values of x will result in a more equal phase fraction of each spinel intermediate. The varying degree of spinel disproportionation may explain why we observe different ratios of t′-spinel to c′-spinel in the presented experiments (Figure 8). For example, experiments collected *ex post facto* after 40 min at each temperature observe more c′-spinel (Figure 1), whereas for *in situ* NPD and SXRD experiments, the samples experience a longer aggregated time at elevated temperatures which results in more conversion to

https://dx.doi.org/10.1021/acs.inorgchem.0c02023
Inorg. Chem. 2020, 59, 13639−13650

the t′-spinel (Figures S1 and S3). This supports control reactions performed with longer dwell times, in which the t′-spinel is often always the observed spinel in XRD results.

The progress of the reaction (ϵ) and the degree of disproportionation (y) determine which $YMnO_3$ polymorph is observed. Figure 5 shows that the stability of $YMnO_3$ is directly influenced by cation defects, specifically the oxidation state of manganese. This observation is supported in previous studies on assisted metathesis reactions to yield $YMnO_{3+\delta}$, where Mn(IV) defects result in the orthorhombic product over h-$YMnO_3$ at temperatures below 850 °C. The value of ϵ in eq 4 influences the composition of the spinel intermediates, specifically, the ratio of lithium to manganese. As more lithium chloride and Y_3O_4Cl forms, the value of y in eq 4 should increase, resulting in a higher relative fraction of *reduced* Mn(II,III) t′-spinel. If less LiCl and Y_3O_4Cl have formed, a greater fraction of *oxidized* Mn(III,IV) c′-spinel will be observed relative to t′-spinel. The observed results suggest that the spinel intermediates react individually with the yttrium oxychloride intermediates to yield different $YMnO_3$ products. Here, Mn(II,III) t′-spinel will yield a product resembling h-$YMnO_{3-\delta}$,[54] and the Mn(III,IV) c′-spinel will result in o-$YMnO_{3+\delta}$, as supported by the calculated phase diagram in Figure 5. While SXRD experiments show more c′-spinel formation than t′-spinel for all three starting polymorphs, a larger weight percent of c′-spinel corresponds to a larger final concentration of o-$YMnO_3$ in the final product. The varying weight percentage of Y_3O_4Cl in the intermediate compositions is indicative of the presence of amorphous intermediates, which likely play a role in reaction pathways, but they are not studied in this work due to the technical challenges of such data analysis. Analysis of *in situ* SXRD data (Figure S2) shows that h-$YMnO_3$ forms as t′-spinel is consumed, providing further evidence to a link between the two phases.

$LiMnO_2$ Polymorph Effects. The identity of the $LiMnO_2$ precursor kinetically controls the composition and relative amount of each intermediate when they react to form $YMnO_3$. The results collectively support a relatively slow reaction pathway to spinel intermediates when starting with the layered m-$LiMnO_2$ or o-$LiMnO_2$ as opposed to starting with the spinel t-$LiMnO_2$. Previous electrochemical studies have identified the mechanism of the layered-to-spinel transition as proceeding slowly to the cubic spinel $LiMn_2O_4$ through a disordered "splayered" intermediate ($R\bar{3}m$ $LiMnO_2$) where manganese moves from manganese oxide layers into the octahedral spinel sites vacated by lithium.[55−57] The presented results proceed through a similar kinetic pathway where the layered precursors react over a broad temperature range to yield the spinel intermediates, although we do not observe the "splayered" intermediate in our diffraction data as this level of resolution is limited within a multiphased sample. Both m-$LiMnO_2$ and o-$LiMnO_2$ are slow to transition to the spinel intermediates, yet the m-$LiMnO_2$ precursor reacts at a lower temperature. The reason for the differences in reactivity between o-$LiMnO_2$ and m-$LiMnO_2$ is due to the degree of structural rearrangement necessary to adopt the spinel structure. As lithium is removed from o-$LiMnO_2$ and m-$LiMnO_2$, manganese must move to fill the octahedral (16d) site in the spinel intermediates. The o-$LiMnO_2$ structure adopts a corrugated rock salt ordering of manganese oxide layers which requires 50% of the manganese atoms to migrate into the octahedral spinel site, whereas in the monoclinic $C2/m$ structure, only 25% of the manganese must move to accommodate the reaction to the spinel intermediate. Thus, starting with m-$LiMnO_2$ results in higher values of ϵ at lower temperatures or a greater value of Y_3O_4Cl and Mn(II,III) t′-spinel at 450 °C when h-$YMnO_3$ forms. As there is more reduced spinel intermediate, the fraction of h-$YMnO_3$ to o-$YMnO_3$ is greatest. In comparison, the value of ϵ is lower when starting with o-$LiMnO_2$, or less Y_3O_4Cl and Mn(II,III) t′-spinel have formed at 500 °C. Then, the amounts of c′-spinel, t′-spinel, r-YOCl, and Y_3O_4Cl all decreased, which results in equal amounts of o-$YMnO_3$ and h-$YMnO_3$.

The reaction pathway starting with t-$LiMnO_2$ yields a different reaction to spinel intermediates. The results in Figure 1g,h denote the same t′-spinel, yet the temperature at which the t′-spinel reacts corresponds to an increase in c′-spinel and not h-$YMnO_3$, which was observed when starting with m-$LiMnO_2$. We hypothesize that the observed t′-spinel resembles a tetragonal spinel closer to $Li_{2-\epsilon}Mn2O_{4-\epsilon/2}$, where $1 < \epsilon < 2$, and not a t′-spinel resembling Mn_3O_4. Thus, we are observing a disproportionation regime that was not present in the diffraction patterns starting from the layered $LiMnO_2$ precursors where a spinel is observed only when $\epsilon \geq 1$. Instead, more o-$LiMnO_2$ and m-$LiMnO_2$ precursors persisted over this $1 < \epsilon < 2$ range when starting with the layered phases, whereas the transition from t-$LiMnO_2$ to spinel intermediates was discrete, supporting the formation of a unique spinel intermediate over this region. This observation results in a pathway where the amount of Mn(III,IV) c′-spinel is greatest, or the value of ϵ is lowest when $YMnO_3$ is observed resulting in more o-$YMnO_3$ relative to h-$YMnO_3$.

$YMnO_3$ Polymorph Selectivity. The DFT-calculated phase diagram in Figure 5 suggests that the phase stability is correlated to the overall concentration of cation defects in the $YMnO_3$ lattice. Specifically, cation vacancies paired with partial oxidation of Mn(III) to Mn(IV) appear to stabilize the orthorhombic phase due to its significantly lower cation vacancy formation energies. This form of cation vacancy-driven stabilization was similarly shown for $CsPbI_3$[58] and $Sc_{1-x}S$.[59] In $YMnO_3$, we predict the critical vacancy concentration which stabilizes the orthorhombic polymorph to be on the order of 2−3%, which is rather low, but it is justified by the very small energy difference between the hexagonal and orthorhombic polymorphs. The calculated concentration is also sensitive to limitations and approximations in our approach, which include the following: 1) the assumption that the defect formation energy does not change with temperature, 2) the assumption of a fixed value of Fermi energy, 3) the prerequisite that structural selectivity in $YMnO_3$ can be modeled assuming an *equal* concentration of cation vacancies, 4) the lack of consideration of anharmonic phonon effects, and 5) the small (uncorrectable) errors inherent to the finite size defect supercell approach. It is also important to note that Figure 5 must be considered from a fixed composition viewpoint; i.e., the phase diagram shows the predicted phase stability as a function of vacancy composition, rather than oxygen partial pressure. This is important in distinguishing the defect mechanisms between the two structures. For example, it is known that hexagonal rare earth manganites $RMnO_{3+\delta}$ synthesized under high oxygen pressure can accommodate excess oxygen via interstitials due to their more open structure.[60] Hence the constructed phase diagram provides a route to understanding thermodynamic stability when approached from a synthesis route in which cation vacancies exist or are likely to form, such as from an intermediate structure containing Mn(IV).

https://dx.doi.org/10.1021/acs.inorgchem.0c02023
Inorg. Chem. 2020, 59, 13639−13650

We anticipate that the inclusion of anharmonic effects could change the calculated Gibbs free energies of the $YMnO_3$ phases considerably at high temperature. This is likely the explanation of the unexpected negative slope of the phase boundary in Figure 5, which is due to the decrease in the free energy difference of the orthorhombic $G(T, P)$ curve with respect to the hexagonal $G(T, P)$ curve at high temperature. Indeed, the heat capacity of h-$YMnO_3$ ($P6_3cm$), which indicates the second derivative of $G(T, P)$ with temperature, underestimates the experimental heat capacity by ~10% at T = 1400 K, as seen in Figure S7. Therefore, anharmonic effects are likely required to explain the proposed entropic stabilization of the hexagonal phase at high temperature that has been experimentally observed.[47,48,61] Nevertheless, we believe that the location of the phase boundary at lower temperature is still a reasonable estimate of the order of magnitude of the critical concentration of cation vacancies which switch the stability between the hexagonal and orthorhombic $YMnO_3$ phases. Even with differing values of Fermi energy within the band gap (Figure S9) we predict this phase boundary to be located in the range $x \simeq 0.022-0.034$ at T = 0 K.

In all of the presented ternary metathesis reactions, long duration reactions yield greater amounts of o-$YMnO_3$ (Figure 6). While the amount of h-$YMnO_3$ and o-$YMnO_3$ depends on the oxidation state of manganese in the spinel intermediates at *short* reaction times, the overall phase stability will reflect the concentration of defects closer to equilibrium, where the overall $YMnO_3$ phase stability will be dependent on the number of defects that are *initially* present in the $LiMnO_2$ precursors. The calculated concentration of cation defects needed to yield o-$YMnO_3$ is small (~2.2%) which supports that even small amounts of impurities or site defects in the bulk $LiMnO_2$ precursors will result in o-$YMnO_{3+\delta}$ at temperatures below 600 °C, if allowed to equilibrate. At 600 °C, h-$YMnO_3$ begins to dominate, which supports previous phase diagrams above 800 °C.[62]

CONCLUSIONS

The reactions of three polymorphs of $LiMnO_2$ with YOCl to form LiCl and $YMnO_3$ are studied using X-ray and neutron diffraction. The reactions form a number of crystalline intermediates, including r-YOCl, Y_3O_4Cl, and two lithium manganese oxide spinel intermediates. The two spinel intermediates, reduced t′-spinel and oxidized c′-spinel, are the result of manganese disproportionation as lithium and oxygen are removed from $LiMnO_2$ over the course of the reaction. DFT-calculated thermochemistry reveals that small changes in manganese oxidation state change the relative stability of the two polymorphs of $YMnO_3$, suggesting that t′-spinel leads to formation of h-$YMnO_3$, while c′-spinel leads to the formation of o-$YMnO_3$. By changing the $LiMnO_2$ precursor, the ratio of reduced to oxidized spinel intermediates changes, which results in different ratios of the observed products. By tuning the composition of these spinel intermediates, the concentration of defects can be synthetically controlled in the resulting $YMnO_3$ products. Paired with additional postsynthesis treatment, these defects can be influenced or removed, which provides increased selectivity in the synthesis of complex oxides. By understanding the role defect-accommodating intermediates play in determining the structure of the final product, routes to new metastable complex solids can be discovered.

ASSOCIATED CONTENT

Supporting Information

The Supporting Information is available free of charge at https://pubs.acs.org/doi/10.1021/acs.inorgchem.0c02023.

Experimental methods, results from control reactions, and additional thermochemical calculations (PDF)

AUTHOR INFORMATION

Corresponding Author

James R. Neilson − *Department of Chemistry, Colorado State University, Fort Collins, Colorado 80523-1872, United States;* orcid.org/0000-0001-9282-5752; Email: james.neilson@colostate.edu

Authors

Paul K. Todd − *Department of Chemistry, Colorado State University, Fort Collins, Colorado 80523-1872, United States;* orcid.org/0000-0001-5409-3634

Allison Wustrow − *Department of Chemistry, Colorado State University, Fort Collins, Colorado 80523-1872, United States*

Rebecca D. McAuliffe − *Chemical Sciences Division, Oak Ridge National Laboratory, Oak Ridge, Tennessee 37831, United States*

Matthew J. McDermott − *Energy Technologies Area, Lawrence Berkeley National Laboratory, Berkeley, California 94720, United States; Department of Materials Science and Engineering, University of California, Berkeley, California 94720, United States*

Gia Thinh Tran − *Department of Chemistry, Colorado State University, Fort Collins, Colorado 80523-1872, United States*

Brennan C. McBride − *Department of Chemistry, Colorado State University, Fort Collins, Colorado 80523-1872, United States*

Ethan D. Boeding − *Chemical Sciences Division, Oak Ridge National Laboratory, Oak Ridge, Tennessee 37831, United States*

Daniel O'Nolan − *Department of Chemistry, Stony Brook University, Stony Brook, New York 11790-3400, United States*

Chia-Hao Liu − *Department of Applied Physics, Columbia University, New York, New York 10027, United States; Condensed Matter Physics and Materials Science Department, Brookhaven National Laboratory, Upton, New York 11973, United States*

Shyam S. Dwaraknath − *Energy Technologies Area, Lawrence Berkeley National Laboratory, Berkeley, California 94720, United States;* orcid.org/0000-0003-0289-2607

Karena W. Chapman − *Department of Chemistry, Stony Brook University, Stony Brook, New York 11790-3400, United States;* orcid.org/0000-0002-8725-5633

Simon J. L. Billinge − *Department of Applied Physics, Columbia University, New York, New York 10027, United States; Condensed Matter Physics and Materials Science Department, Brookhaven National Laboratory, Upton, New York 11973, United States;* orcid.org/0000-0002-9734-4998

Kristin A. Persson − *Energy Technologies Area, Lawrence Berkeley National Laboratory, Berkeley, California 94720, United States; Department of Materials Science and Engineering, University of California, Berkeley, California 94720, United States;* orcid.org/0000-0003-2495-5509

Ashfia Huq − *Neutron Scattering Division, Oak Ridge National Laboratory, Oak Ridge, Tennessee 37831, United States*

https://dx.doi.org/10.1021/acs.inorgchem.0c02023
Inorg. Chem. 2020, 59, 13639−13650

Gabriel M. Veith − *Chemical Sciences Division, Oak Ridge National Laboratory, Oak Ridge, Tennessee 37831, United States;* orcid.org/0000-0002-5186-4461

Complete contact information is available at: https://pubs.acs.org/10.1021/acs.inorgchem.0c02023

Author Contributions

○P.K.T., A.W., R.D.M., and M.J.M. contributed equally to this work.

Author Contributions

P.K.T., A.W., R.D.M., and E.D.B. synthesized and characterized precursors. P.K.T. and A.W. performed and analyzed ex situ reactions. P.K.T., A.W., G.T.T., and B.C.M. performed SXRD experiments. D.O. and K.C. assisted with using the gradient furnace, and C.L. wrote scripts to assist with SXRD collection under the supervision of S.B. A.W. and P.K.T. analyzed SXRD data. R.D.M. performed and analyzed NPD experiments assisted by A.H. M.J.M., S.S.D., and K.A.P. performed calculations relating the stability of the $YMnO_3$ polymorphs. P.K.T., A.W., R.D.M., and M.J.M. wrote the manuscript with the guidance of J.R.N., G.M.V., and K.A.P.

Notes

The authors declare no competing financial interest.

■ ACKNOWLEDGMENTS

This work was supported as part of GENESIS: A Next Generation Synthesis Center, an Energy Frontier Research Center funded by the U.S. Department of Energy, Office of Science, Basic Energy Sciences under Award Number DE-SC0019212. This research used resources at beamline 28-ID-2 of the National Synchrotron Light Source II, a U.S. Department of Energy (DOE) Office of Science User Facility operated for the DOE Office of Science by Brookhaven National Laboratory under Contract No. DE-SC0012704. Research was performed at Oak Ridge National Laboratory (ORNL), managed by UT Battelle, LLC for the U.S. Department of Energy (DOE) under contract DE-AC05-00OR22725. A portion of this research used resources at the Spallation Neutron Source, a DOE Office of Science User Facility operated by the Oak Ridge National Laboratory. We acknowledge Melanie Kirkham and Qiang Zhang at POWGEN for their assistance. We would like to acknowledge C. Rom for his assistance with SXRD experiments. We would also like to acknowledge the facilities at 17-BM-B at the Advanced Photon Source at Argonne National Laboratory and, in particular, the support of A. Yakovenko and W. Wu. Theoretical calculations completed in this research used resources of the National Energy Research Scientific Computing Center (NERSC), a U.S. Department of Energy Office of Science User Facility operated under Contract No. DE-AC02-05CH11231. J.R.N. acknowledges partial support from a Sloan Research Fellowship.

■ REFERENCES

(1) Stein, A.; Keller, S. W.; Mallouk, T. E. Turning Down the Heat: Design and Mechanism in Solid-State Synthesis. *Science* **1993**, *259*, 1558−1564.

(2) Soderholm, L.; Mitchell, J. F. Perspective: Toward "synthesis by design": Exploring atomic correlations during inorganic materials synthesis. *APL Mater.* **2016**, *4*, 053212.

(3) Rouxel, J. Chimie douce with solid precursors, past and present. *Solid State Ionics* **1996**, *84*, 141−149.

(4) Gopalakrishnan, J. Chimie Douce Approaches to the Synthesis of Metastable Oxide Material. *Chem. Mater.* **1995**, *7*, 1265−1275.

(5) Vitoux, L.; Guignard, M.; Suchomel, M. R.; Pramudita, J. C.; Sharma, N.; Delmas, C. The Na_xMoO_2 Phase Diagram ($1/2 \leq x < 1$): An Electrochemical Devil's Staircase. *Chem. Mater.* **2017**, *29*, 7243−7254.

(6) Poeppelmeier, K. R.; Kipp, D. O. Cation Replacement in α-$LiAlO_2$. *Inorg. Chem.* **1988**, *27*, 766−767.

(7) Gillan, E. G.; Kaner, R. B. Synthesis of Refractory Ceramics via Rapid Metathesis Reactions between Solid-State Precursors. *Chem. Mater.* **1996**, *8*, 333−343.

(8) Martinolich, A. J.; Neilson, J. R. Toward Reaction-by-Design: Achieving Kinetic Control of Solid State Chemistry with Metathesis. *Chem. Mater.* **2017**, *29*, 479−489.

(9) Todd, P. K.; Neilson, J. R. Selective Formation of Yttrium Manganese Oxides through Kinetically Competent Assisted Metathesis Reactions. *J. Am. Chem. Soc.* **2019**, *141*, 1191−1195.

(10) Armstrong, A. R.; Bruce, P. G. Synthesis of layered $LiMnO_2$ as an electrode for rechargeable lithium batteries. *Nature* **1996**, *381*, 499−500.

(11) Croguennec, L.; Deniard, P.; Brec, R.; Lecerf, A. Preparation, physical and structural characterization of $LiMnO_2$ samples with variable cationic disorder. *J. Mater. Chem.* **1995**, *5*, 1919.

(12) Mosbah, A.; Verbaere, A.; Tournoux, M. Phases $Li_xMnO_{2\lambda}$ rattachees au type spinelle. *Mater. Res. Bull.* **1983**, *18*, 1375−1381.

(13) Wendlandt, W. W. The thermal decomposition of yttrium, scandium, and some rare-earth chloride hydrates. *J. Inorg. Nucl. Chem.* **1957**, *5*, 118−122.

(14) Tarascon, J.; Guyomard, D. Li Metal-Free Rechargeable Batteries Based on $Li_{1+x}Mn_2O_4$ Cathodes ($0 \leq x \leq 1$) and Carbon Anodes. *J. Electrochem. Soc.* **1991**, *138*, 2864−2868.

(15) Wang, M.; Navrotsky, A. $LiMO_2$ (M = Mn, Fe, and Co): Energetics, polymorphism and phase transformation. *J. Solid State Chem.* **2005**, *178*, 1230−1240.

(16) Fuchs, B.; Kemmler-Sack, S. Synthesis of $LiMnO_2$ and $LiFeO_2$ in molten Li halides. *Solid State Ionics* **1994**, *68*, 279−285.

(17) O'Nolan, D.; Huang, G.; Kamm, G. E.; Grenier, A.; Liu, C.-H.; Todd, P. K.; Wustrow, A.; Thinh Tran, G.; Montiel, D.; Neilson, J. R.; Billinge, S. J. L.; Chupas, P. J.; Thornton, K. S.; Chapman, K. W. A thermal-gradient approach to variable-temperature measurements resolved in space. *J. Appl. Crystallogr.* **2020**, *53*, 662.

(18) Ashiotis, G.; Deschildre, A.; Nawaz, Z.; Wright, J. P.; Karkoulis, D.; Picca, F. E.; Kieffer, J. The fast azimuthal integration Python library: *pyFAI*. *J. Appl. Crystallogr.* **2015**, *48*, 510−519.

(19) Pathak, P.; Vasavada, N. Thermal expansion of NaCl, KCl and CsBr by X-ray diffraction and the law of corresponding states. *Acta Crystallogr., Sect. A: Cryst. Phys., Diffr., Theor. Gen. Crystallogr.* **1970**, *26*, 655−658.

(20) Kirkham, M.; Heroux, L.; Ruiz-Rodriguez, M.; Huq, A. AGES: Automated Gas Environment System for in situ neutron powder diffraction. *Rev. Sci. Instrum.* **2018**, *89*, 092904.

(21) Chupas, P. J.; Chapman, K. W.; Kurtz, C.; Hanson, J. C.; Lee, P. L.; Grey, C. P. A versatile sample-environment cell for non-ambient X-ray scattering experiments. *J. Appl. Crystallogr.* **2008**, *41*, 822−824.

(22) Kresse, G.; Furthmüller, J. Efficient iterative schemes for ab initio total-energy calculations using a plane-wave basis set. *Phys. Rev. B: Condens. Matter Mater. Phys.* **1996**, *54*, 11169−11186.

(23) Perdew, J. P.; Burke, K.; Ernzerhof, M. Generalized Gradient Approximation Made Simple. *Phys. Rev. Lett.* **1996**, *77*, 3865−3868.

(24) Wang, Y.; Fu, Z.-W.; Yue, X.-L.; Qin, Q.-Z. Electrochemical Reactivity Mechanism of Ni_3N with Lithium. *J. Electrochem. Soc.* **2004**, *151*, E162.

(25) Hautier, G.; Ong, S. P.; Jain, A.; Moore, C. J.; Ceder, G. Accuracy of density functional theory in predicting formation energies of ternary oxides from binary oxides and its implication on phase stability. *Phys. Rev. B: Condens. Matter Mater. Phys.* **2012**, *85*, 155208.

(26) Blöchl, P. E. Projector augmented-wave method. *Phys. Rev. B: Condens. Matter Mater. Phys.* **1994**, *50*, 17953−17979.

(27) Kresse, G.; Joubert, D. From ultrasoft pseudopotentials to the projector augmented-wave method. *Phys. Rev. B: Condens. Matter Mater. Phys.* **1999**, *59*, 1758−1775.
(28) Ong, S. P.; Richards, W. D.; Jain, A.; Hautier, G.; Kocher, M.; Cholia, S.; Gunter, D.; Chevrier, V. L.; Persson, K. A.; Ceder, G. Python Materials Genomics (pymatgen): A robust, open-source python library for materials analysis. *Comput. Mater. Sci.* **2013**, *68*, 314−319.
(29) Togo, A.; Tanaka, I. First principles phonon calculations in materials science. *Scr. Mater.* **2015**, *108*, 1−5.
(30) Persson, K. *Materials Data on $YMnO_3$ (SG:185) by Materials Project*; 2015; DOI: 10.17188/1194392.
(31) Persson, K. *Materials Data on $YMnO_3$ (SG:194) by Materials Project*; 2014; DOI: 10.17188/1194088.
(32) Zhou, Z.; Guo, L.; Ye, F. Hydrothermal synthesis, magnetism and resistivity of orthorhombic perovskite manganates $Y_{1-x}Ca_xMnO_3$ (x = 0, 0.07, 0.55, 0.65). *J. Alloys Compd.* **2013**, *571*, 123−131.
(33) Jain, A.; Ong, S. P.; Hautier, G.; Chen, W.; Richards, W. D.; Dacek, S.; Cholia, S.; Gunter, D.; Skinner, D.; Ceder, G.; Persson, K. A. Commentary: The Materials Project: A materials genome approach to accelerating materials innovation. *APL Mater.* **2013**, *1*, 011002.
(34) Muñoz, A.; Alonso, J. A.; Martínez-Lope, M. J.; Casáis, M. T.; Martínez, J. L.; Fernández-Díaz, M. T. Magnetic structure of hexagonal $RMnO_3$. *Phys. Rev. B: Condens. Matter Mater. Phys.* **2000**, *62*, 9498−9510.
(35) Muñoz, A.; Alonso, J. a.; Casais, M. T.; Martínez-Lope, M. J.; Martínez, J. L.; Fernández-Díaz, M. T. The magnetic structure of $YMnO_3$ perovskite revisited. *J. Phys.: Condens. Matter* **2002**, *14*, 3285−3294.
(36) Horton, M. K.; Montoya, J. H.; Liu, M.; Persson, K. A. High-throughput prediction of the ground-state collinear magnetic order of inorganic materials using Density Functional Theory. *npj Computational Materials* **2019**, *5*, 64.
(37) Vinet, P.; Rose, J. H.; Ferrante, J.; Smith, J. R. Universal features of the equation of state of solids. *J. Phys.: Condens. Matter* **1989**, *1*, 1941−1963.
(38) Freysoldt, C.; Neugebauer, J.; Van de Walle, C. G. Fully Ab Initio Finite-Size Corrections for Charged-Defect Supercell Calculations. *Phys. Rev. Lett.* **2009**, *102*, 016402.
(39) Freysoldt, C.; Grabowski, B.; Hickel, T.; Neugebauer, J.; Kresse, G.; Janotti, A.; Van de Walle, C. G. First-principles calculations for point defects in solids. *Rev. Mod. Phys.* **2014**, *86*, 253−305.
(40) Broberg, D.; Medasani, B.; Zimmermann, N. E.; Yu, G.; Canning, A.; Haranczyk, M.; Asta, M.; Hautier, G. PyCDT: A Python toolkit for modeling point defects in semiconductors and insulators. *Comput. Phys. Commun.* **2018**, *226*, 165−179.
(41) Mathew, K.; et al. Atomate: A high-level interface to generate, execute, and analyze computational materials science workflows. *Comput. Mater. Sci.* **2017**, *139*, 140−152.
(42) Tofield, B. C.; Scott, W. R. Oxidative nonstoichiometry in perovskites, an experimental survey; the defect structure of an oxidized lanthanum Manganite by powder neutron diffraction. *J. Solid State Chem.* **1974**, *10*, 183−194.
(43) Van Roosmalen, J. A. M.; Cordfunke, E.; Helmholdt, R.; Zandbergen, H. The Defect Chemistry of $LaMnO_{3\pm\delta}$: 2. Structural Aspects of $LaMnO_{3+\delta}$. *J. Solid State Chem.* **1994**, *110*, 100−105.
(44) Alonso, J. A.; Martínez-lope, M. J.; Casais, M. T.; Macmanus-Driscoll, J. L.; de Silva, P. S. I. P. N.; Cohen, L. F.; Fernández-díaz, M. T. Non-stoichiometry, structural defects and properties of $LaMnO_{3+\delta}$ with high δ values ($0.11 \leq \delta \leq 0.29$). *J. Mater. Chem.* **1997**, *7*, 2139−2144.
(45) Dabrowski, B.; Kolesnik, S.; Baszczuk, A.; Chmaissem, O.; Maxwell, T.; Mais, J. Structural, transport, and magnetic properties of $RMnO_3$ perovskites (R = La, Pr, Nd, Sm, Eu, Dy). *J. Solid State Chem.* **2005**, *178*, 629−637.
(46) Todd, P. K.; Smith, A. M. M.; Neilson, J. R. Yttrium Manganese Oxide Phase Stability and Selectivity Using Lithium Carbonate Assisted Metathesis Reactions. *Inorg. Chem.* **2019**, *58*, 15166−15174.
(47) Brinks, H.; Fjellvåg, H.; Kjekshus, A. Synthesis of Metastable Perovskite-type $YMnO_3$ and $HoMnO_3$. *J. Solid State Chem.* **1997**, *129*, 334−340.
(48) Bergum, K.; Okamoto, H.; Fjellvåg, H.; Grande, T.; Einarsrud, M.-A.; Selbach, S. M. Synthesis, structure, and magnetic properties of nanocrystalline $YMnO_3$. *Dalton Trans.* **2011**, *40*, 7583.
(49) Gibbs, A. S.; Knight, K. S.; Lightfoot, P. High-temperature phase transitions of hexagonal $YMnO_3$. *Phys. Rev. B: Condens. Matter Mater. Phys.* **2011**, *83*, 094111.
(50) Garcia, E.; Corbett, J. D.; Ford, J. E.; Vary, W. J. Low-Temperature Routes to New Structures for Yttrium, Holmium, Erbium, and Thulium Oxychlorides. *Inorg. Chem.* **1985**, *24*, 494−498.
(51) Ohzuku, T.; Kitagawa, M.; Hirai, T. Electrochemistry of Manganese Dioxide in Lithium Nonaqueous Cell: III. X-Ray Diffractional Study on the Reduction of Spinel-Related Manganese Dioxide. *J. Electrochem. Soc.* **1990**, *137*, 769−775.
(52) Liu, T.; et al. Correlation between manganese dissolution and dynamic phase stability in spinel-based lithium-ion battery. *Nat. Commun.* **2019**, *10*, 4721.
(53) Sugiyama, J.; Atsumi, T.; Hioki, T.; Noda, S.; Kamegashira, N. Nonstoichiometry and defect structure of spinel $LiMn_2O_{4-\delta}$. *J. Power Sources* **1997**, *68*, 641−645.
(54) Atsumi, T.; Ohgushi, T.; Namikata, H.; Kamegashira, N. Oxygen nonstoichiometry of $LnMnO_{3-\delta}$ (Ln = La, Pr, Nd, Sm and Y). *J. Alloys Compd.* **1997**, *252*, 67−70.
(55) Reed, J.; Ceder, G.; Van Der Ven, A. Layered-to-spinel phase transition in Li_xMnO_2. *Electrochem. Solid-State Lett.* **2001**, *4*, A78.
(56) Armstrong, A. R.; Dupre, N.; Paterson, A. J.; Grey, C. P.; Bruce, P. G. Combined neutron diffraction, NMR, and electrochemical investigation of the layered-to-spinel transformation in $LiMnO_2$. *Chem. Mater.* **2004**, *16*, 3106−3118.
(57) Armstrong, A. R.; Paterson, A. J.; Dupré, N.; Grey, C. P.; Bruce, P. G. Structural evolution of layered $Li_xMn_yO_2$: Combined neutron, NMR, and electrochemical study. *Chem. Mater.* **2007**, *19*, 1016−1023.
(58) Kye, Y.-H.; Yu, C.-J.; Jong, U.-G.; Ri, K.-C.; Kim, J.-S.; Choe, S.-H.; Hong, S.-N.; Li, S.; Wilson, J. N.; Walsh, A. Vacancy-Driven Stabilization of the Cubic Perovskite Polymorph of CsPbI3. *J. Phys. Chem. C* **2019**, *123*, 9735−9744.
(59) Burdett, J. K. Electronic Structure and Properties of Solids. *J. Phys. Chem.* **1996**, *100*, 13263−13274.
(60) Skjaervø, S. L.; Sommer, S.; Nørby, P.; Bøjesen, E. D.; Grande, T.; Iversen, B. B.; Einarsrud, M.-A. Formation mechanism and growth of $MNbO_3$, M = K, Na by in situ X-ray diffraction. *J. Am. Ceram. Soc.* **2017**, *100*, 3835−3842.
(61) Chen, X.-J.; Struzhkin, V. V.; Wu, Z.; Somayazulu, M.; Qian, J.; Kung, S.; Christensen, A. N.; Zhao, Y.; Cohen, R. E.; Mao, H.-k.; Hemley, R. J. Hard superconducting nitrides. *Proc. Natl. Acad. Sci. U. S. A.* **2005**, *102*, 3198−3201.
(62) Balakirev, V. F.; Vedmid, L. B.; Yankin, a. M.; Fedorova, O. M.; Golikov, Y. V. Heterogeneous phase equilibria in the Tb-Mn-O system. *Inorg. Mater.* **2006**, *42*, 1230−1235.

https://dx.doi.org/10.1021/acs.inorgchem.0c02023
Inorg. Chem. 2020, 59, 13639−13650